Author(s): Lehtovaara, Lauri & Havu, Ville & Puska, Martti J.

Title: All-electron density functional theory and time-dependent density functional theory with high-order finite elements

Year: 2009

Version: Final published version

Please cite the original version:

Lehtovaara, Lauri & Havu, Ville & Puska, Martti J. 2009. All-electron density functional theory and time-dependent density functional theory with high-order finite elements. The Journal of Chemical Physics. Volume 131, Issue 5. 054103/1-10. ISSN 1089-7690 (electronic). DOI: 10.1063/1.3176508.

All-electron density functional theory and time-dependent density functional theory with high-order finite elements

Lauri Lehtovaara, Ville Havu, and Martti Puska

Citation: The Journal of Chemical Physics **131**, 054103 (2009); doi: 10.1063/1.3176508
View online: http://dx.doi.org/10.1063/1.3176508
View Table of Contents: http://scitation.aip.org/content/aip/journal/jcp/131/5?ver=pdfcov
Published by the AIP Publishing

All-electron density functional theory and time-dependent density functional theory with high-order finite elements

Lauri Lehtovaara,[1,a)] Ville Havu,[1,2] and Martti Puska[1]
[1]*Department of Applied Physics/COMP, Helsinki University of Technology, P.O. Box 110, FIN-02015 TKK, Finland*
[2]*Institute of Mathematics, Helsinki University of Technology, P.O. Box 110, FIN-02015 TKK, Finland*

(Received 17 February 2009; accepted 23 June 2009; published online 3 August 2009)

We present for static density functional theory and time-dependent density functional theory calculations an all-electron method which employs high-order hierarchical finite-element bases. Our mesh generation scheme, in which structured atomic meshes are merged to an unstructured molecular mesh, allows a highly nonuniform discretization of the space. Thus it is possible to represent the core and valence states using the same discretization scheme, i.e., no pseudopotentials or similar treatments are required. The nonuniform discretization also allows the use of large simulation cells, and therefore avoids any boundary effects. © *2009 American Institute of Physics*. [DOI: 10.1063/1.3176508]

I. INTRODUCTION

The density functional theory (DFT) has become the workhorse in electronic structure theory.[1] Its success derives from the ability to produce accurate results with reasonable computational effort. Instead of solving for the many-body wave function it relies on Hohenberg–Kohn[2] theorem, which states that all ground-state properties—most importantly the total energy—are functionals of the electron density. Actually, the total energy functional is not exactly known, but there exists several approximations, the accuracy of which can be systematically improved according to the demands of the applications in question.[3,4] The most important issue is that the number of dimensions in a problem does not depend on the number of electrons, and thus DFT scales much better than many-body wave function methods, up to hundreds or thousands of atoms on the present supercomputers.

The DFT is bound to the ground-state properties and cannot be used to explore excited states. This drawback can be overcome by using the time-dependent DFT (TDDFT).[5] It is based on the Runge–Gross[6] theorem, which states that (physically) different external potentials (e.g., those due to laser fields) lead to different time-evolutions of the density. The present functionals for TDDFT are known to be unable to describe certain phenomena, such as charge transfer excitations. However, in recent years it has been successfully applied to describe several other problems, for example, the optical absorption spectra of a broad variety of systems, the nonlinear optical response (e.g., harmonic generation) of atoms and molecules, and coherent control of molecules by laser fields.[5]

For numerical solution, the partial differential equations arising from DFT and TDDFT must be discretized in space. In the present-day codes, the most popular choices are atomic orbital bases,[7–9] planewaves,[10,11] and uniform real-space grids.[12,13] In the atomic orbital bases the solution is represented as a linear combination of atomic solutions, which can be accurate (e.g., numerical atomic orbitals[7]) or approximate (e.g., Gaussians[8]). These bases are widely used and can be very fast and efficient. However, the atomic orbital bases are sensitive to the type of the problem in the sense that an efficient discretization for the ground-state properties is not well-suited for the calculation of optical absorption spectra. In particular, when the solution is not representable as slightly perturbed atomic solutions the atomic orbital bases become unfavourable. For example, this can happen in the case of nonlinear time-dependent phenomena.

The plane-wave bases and uniform real-space grids (i.e., the finite-difference method) are both uniform discretizations of the space and closely related to each other through the Fourier transform. These discretizations are not dependent on the type of the problem, but they require a large number of degrees of freedom (DOFs). Especially, the core regions around nuclei, where solutions have very sharp features, cannot be represented well by uniform discretization, but pseudopotentials[14–16] or similar treatments (e.g., projector-augmented wave method[17]) must be employed. The pseudopotentials lead to additional parameters and may be hard to construct accurately for certain types of atoms, e.g., transition metals. Another drawback in uniform discretizations is their inability to adapt to the underlying geometry of the atoms. For example, sparse matter interstitial regions should require much less DOFs than regions near atoms. This is also the case in simulations of nonlinear time-dependent phenomena, where the distant regions in space should still be accounted for but the solution is smooth in this region so that the discretization can be coarse.

The finite-element basis[18,19] is a linear combination of continuous, piece-wise polynomials and provides a nonuniform real-space discretization of the space. It inherits the good properties of the real-space methods, such as flexible boundary conditions and efficient parallelization via domain decomposition, while still allowing nonuniform discretization of the space. In this paper, we use high-order hierarchi-

[a)]Electronic mail: lauri.lehtovaara@hut.fi.

cal finite elements, which (i) provide a better rate of convergence than low-order elements and (ii) result in better conditioned systems of linear equations than the nodal-based elements of the same order. As finite elements can adapt to the local feature size, they can be used to describe solutions of core and valence electrons equally well. Also naturally, they are adaptable to the geometry of the system to avoid overdiscretization. The finite-element basis is also variational, such as planewaves and atomic bases, which is not the case for finite-difference discretizations. The finite-element basis is extensively used in civil and mechanical engineering, and in many fields it has surpassed finite-difference methods.[20] There exists several earlier implementations of the finite-element methodology to electronic structure calculations.[21–29] However, none of these uses high-order hierarchical elements on unstructured meshes or apply the method to TDDFT. The closest work to our approach is the spectral element method implementation of Batcho.[22] The spectral element method uses high-order tensor product bases, which enable fast evaluation of matrix elements and provide good convergence rates. However, the element types are restricted to brick (i.e., parallelepiped) elements and mapped brick elements (i.e., coordinate transformations of brick elements).

The rest of the paper is structured as follows. In the next section, we briefly review the DFT, linear-response TDDFT, and finite-element method. We also describe our mesh generation algorithm. In Sec. III, we show several examples of applying our DFT and linear-response TDDFT method to small molecules (CO, Na_2, C_6H_6) and discuss the convergence of the method. In the final section, we draw the conclusions and set directions for future research.

II. THEORY

A. DFT

In the DFT, the total energy $E[n(\mathbf{r})]$ is a functional of the electron density $n(\mathbf{r})$, and the ground state of the system is found by minimizing it. However, the functional is not known in general and must be approximated. This is usually done by employing the Kohn–Sham[30] scheme where the functional is divided into four parts

$$E[n] = T_s[n] + \int d^3r n(\mathbf{r}) v_{\text{ext}}(\mathbf{r}) + U[n] + E_{\text{xc}}[n], \tag{1}$$

where $T_s[n]$ is the kinetic energy of the noninteracting electron system with density $n(\mathbf{r})$, $\int d^3r n(\mathbf{r}) v_{\text{ext}}(\mathbf{r})$ is the interaction energy with an external field (usually that due to the ions), $U[n]$ is the mean electron-electron repulsion energy (Hartree energy), and $E_{\text{xc}}[n]$ is the electron exchange-correlation energy functional. The first three parts are known but the last one, the exchange-correlation functional, is not, and the quality of its approximation is the key to accurate results. The Kohn–Sham[30] scheme uses a set of orthonormal auxiliary functions $\psi_k(\mathbf{r})$, i.e., the Kohn–Sham[30] orbitals, which satisfy

$$n(\mathbf{r}) = \sum_{k=1}^{N_{\text{states}}} f_k |\psi_k(\mathbf{r})|^2, \tag{2}$$

where f_k are the occupation numbers, and N_{states} is the number of occupied Kohn–Sham[30] orbitals. By taking the functional derivative of the energy functional with respect to these functions, we obtain the Kohn–Sham[30] equations

$$\hat{H}_{\text{KS}} \psi_k(\mathbf{r}) = \left[-\frac{\hbar^2}{2m_e} \nabla^2 + v_{\text{eff}}(\mathbf{r}) \right] \psi_k(\mathbf{r}) = \epsilon_k \psi_k(\mathbf{r}), \tag{3}$$

where

$$v_{\text{eff}}(\mathbf{r}) = v_H[n](\mathbf{r}) + v_{\text{xc}}[n](\mathbf{r}) + v_{\text{ext}}(\mathbf{r}), \tag{4}$$

is the effective potential, and

$$v_H[n](\mathbf{r}) = \frac{e^2}{4\pi\varepsilon_0} \int d^3r' \frac{n(\mathbf{r}')}{|\mathbf{r} - \mathbf{r}'|}, \tag{5}$$

is the Hartree potential. Furthermore, $v_{\text{xc}}[n](\mathbf{r})$ is the exchange-correlation potential, and $v_{\text{ext}}(\mathbf{r})$ is the external potential, which is usually a sum of electron-nucleus interactions, i.e.,

$$v_{\text{ext}}(\mathbf{r}) = \frac{-e^2}{4\pi\varepsilon_0} \sum_{a=1}^{N_{\text{nuclei}}} \frac{Z_a}{|\mathbf{r} - \mathbf{r}_a|}, \tag{6}$$

where Z_a is the atomic number and $\mathbf{r}_a$ is the position of the nucleus a. N_{nuclei} is the number of nuclei in the system. In the three-dimensional space $\mathbb{R}^3$, the Hartree potential can be rewritten as the solution of the Poisson equation

$$\nabla^2 v_H(\mathbf{r}) = -4\pi \frac{e^2}{4\pi\varepsilon_0} n(\mathbf{r}), \tag{7}$$

where the boundary condition for isolated systems is $v_H \to 0$ when $|\mathbf{r}| \to \infty$. (Also periodic and other boundary conditions are possible but are not discussed in this paper.)

As the Hartree potential, the density and thus the Kohn–Sham[30] wave functions vanish at the infinity (or in practice at the boundary $\partial\Omega$ of the computational domain Ω), the above Eqs. (3) and (7) can be cast into the weak variational formulation using integration by parts, i.e.,

$$\begin{aligned} \langle \Phi | \hat{H}_{\text{KS}} | \psi_k \rangle &= \int_{\mathbb{R}^3} \Phi(\mathbf{r}) \left[\frac{-\hbar^2}{2m_e} \nabla^2 + v_{\text{eff}}(\mathbf{r}) \right] \psi_k(\mathbf{r}) d^3r \\ &= \int_{\mathbb{R}^3} \left[\frac{\hbar^2}{2m_e} \nabla \Phi(\mathbf{r}) \cdot \nabla \psi_k(\mathbf{r}) \right. \\ &\quad \left. + \Phi(\mathbf{r}) v_{\text{eff}}(\mathbf{r}) \psi_k(\mathbf{r}) d^3r \right], \end{aligned} \tag{8}$$

and

$$\begin{aligned} \langle \Phi | \nabla^2 | v_H \rangle &= \int_{\mathbb{R}^3} \Phi(\mathbf{r}) \nabla^2 v_H(\mathbf{r}) d^3r \\ &= -\int_{\mathbb{R}^3} \nabla \Phi(\mathbf{r}) \cdot \nabla v_H(\mathbf{r}) d^3r, \end{aligned} \tag{9}$$

where $\Phi(\mathbf{r})$ is a test function which has a square integrable gradient $\nabla\Phi(\mathbf{r})$. The weak formulation is required by the

finite-element method, and in practice, $\Phi(\mathbf{r})$ will be a finite-element basis function [in the so-called Ritz–Galerkin method,[31] see Eq. (21)].

As the Hartree potential for charged systems decays slowly as r^{-1}, we have applied counter charges to neutralize the density. The counter charges are added to the electronic density $n(r)$ in Eq. (9) and are then cancelled in Eq. (8) by the corresponding analytically calculated potential. This provides the r^{-2} decay of the Hartree potential, which is sufficient for our purposes. However, if required, higher order (e.g., dipole and quadrupole) corrections can be applied as well.[22]

B. Linear-response TDDFT

In the TDDFT, there exists no variational principle, but the quantum mechanical action

$$A[\psi] = \int_{t_0}^{t_1} dt \langle \psi(t) | i\hbar \frac{\partial}{\partial t} - \hat{H}(t) | \psi(t) \rangle, \tag{10}$$

provides an analogous quantity to the total energy of the ground-state DFT. The time-dependent Kohn–Sham[30] Schrödinger equation reads as

$$i\hbar \frac{\partial}{\partial t} \psi_k(\mathbf{r},t) = \left[-\frac{\hbar^2}{2m_e} \nabla^2 + v_{\mathrm{eff}}(n)(\mathbf{r},t) \right] \psi_k(\mathbf{r},t). \tag{11}$$

This equation is an initial value problem and can be solved using a time-propagation scheme.[32] However, if the external perturbation is small, the density response of the system can be written as a series

$$n(\mathbf{r},\omega) = n^{(0)}(\mathbf{r}) + n^{(1)}(\mathbf{r},\omega) + n^{(2)}(\mathbf{r},\omega) + \ldots, \tag{12}$$

with the linear-response term

$$n^{(1)}(\mathbf{r},\omega) = \int d^3r' \chi(\mathbf{r},\mathbf{r}',\omega) v^{(1)}(\mathbf{r}',\omega). \tag{13}$$

Above, χ is the linear-response function and $v^{(1)}$ is the external perturbation (e.g., a laser field). The transitions can be found by finding the poles of the response function $\chi(\mathbf{r},\mathbf{r}',\omega)$. However, if we are interested only in the excitation energies and corresponding oscillator strengths, we can use the so-called Casida[33,34] method. He showed that the problem can be solved as an eigenvalue equation

$$\sum_{j'k'} [\delta_{jk}\delta_{j'k'}\epsilon_{jk}^2 + 2\sqrt{f_{kj}\epsilon_{jk}f_{k'j'}\epsilon_{j'k'}} K_{jk,j'k'}] \gamma_{j'k'} = \Omega^2 \gamma_{jk}, \tag{14}$$

where $f_{kj}=f_k-f_j$, $\epsilon_{jk}=\epsilon_j-\epsilon_k$, and the coupling matrix

$$K_{jk,j'k'}(\omega) = \int d^3\mathbf{r} \int d^3\mathbf{r}' \psi_j^*(\mathbf{r}) \psi_k(\mathbf{r}) \psi_{j'}(\mathbf{r}') \psi_{k'}^*(\mathbf{r}') \times \left[\frac{e^2}{4\pi\varepsilon_0} \frac{1}{|\mathbf{r}-\mathbf{r}'|} + f_{\mathrm{xc}}(\mathbf{r},\mathbf{r}',\omega) \right]. \tag{15}$$

Moreover,

$$f_{\mathrm{xc}}(\mathbf{r}\omega,\mathbf{r}'\omega') = \frac{\delta v_{\mathrm{xc}}(\mathbf{r},\omega)}{\delta n(\mathbf{r}',\omega')}, \tag{16}$$

is the exchange-correlation kernel. The oscillator strengths are then

$$\tilde{f}_{x/y/z}^{(m)} = \frac{2m}{\hbar^2 e^2} \left| \sum_{jk}^{f_k > f_j} (\mu_{jk})_{x/y/z} \sqrt{(f_k - f_j)(\epsilon_j - \epsilon_k)} \gamma_{jk}^{(m)} \right|^2, \tag{17}$$

where $(\mu_{jk})_{x/y/z}$ is the $x/y/z$ component of the dipole moment vector between the Kohn–Sham[30] states k and j, and the index (m) refers to the mth transition.

1. Confinement potential

The linear-response Kohn–Sham[30] equations use the Kohn–Sham[30] states as a basis. Above the ionization limit of the system, the spectrum becomes continuous causing numerical problems. The eigenvalues of the discretized problem bunch together just above the ionization limit. For a practical calculation this is not desirable because certain transitions have very many different contributions due to the eigenstates in the Kohn–Sham[30] continuum and the importance of most of them is minor because the states have a relatively small amplitude near the molecule.

To spread the eigenvalue spectrum above the ionization limit, and to increase the relative importance of the relevant unoccupied states, we use a modified Kohn–Sham[30] basis $\{\tilde{\psi}_k(\mathbf{r})\}$. The basis is constructed by applying an auxiliary confinement potential in the ground-state calculation. The choice of the potential is in principle arbitrary, but in order to fill the above requirements, we have chosen the form

$$v_{\mathrm{conf}}(\mathbf{r}) = \begin{cases} \frac{1}{2} k_c |r_{\min}(\mathbf{r}) - R_c|^2, & \text{if } r_{\min}(\mathbf{r}) > R_c, \\ 0, & \text{otherwise}, \end{cases} \tag{18}$$

where $r_{\min}(\mathbf{r}) = \min_{R_a} |r - R_a|$ is the distance to the closest atom, and k_c and R_c are parameters to be chosen. Thus, the auxiliary potential is zero close to the atoms but becomes gradually more repulsive further away. Far away from the system, the auxiliary potential is a spherically symmetric harmonic potential. Now, all states are bound.

After the ground-state calculation with the auxiliary confinement potential the resulting Kohn–Sham[30] states $\{\tilde{\psi}_k(\mathbf{r})\}$ are taken as the new basis, the auxiliary confinement potential is removed, and the ground-state calculation is repeated in the new basis. Finally, the linear-response calculation is carried out in the new basis.

Introducing the auxiliary confinement potential allows us to balance between the number of unoccupied states and the quality of the low energy part of the spectrum. We want to stress out that this is purely a mathematical trick in order to alter the basis of the linear-response calculation in such a way that the low energy transitions converge more quickly. The physics is not altered. The calculated linear-response spectrum with and without an auxiliary confinement potential should give the same result when all the Kohn–Sham[30] states (occupied and unoccupied) are used as they span the same original finite-element space V_h. Also, as the confine-

ment potential determines the linear-response basis, the final result of a converged calculation is independent of the original basis where the Kohn–Sham[30] states were solved, e.g., converged atomic orbital and real-space calculations should give the same result.

The choice of the parameters R_c and k_c is not an obvious task and some testing is required to find appropriate values. However, the testing can be done as a linear problem by fixing the density, because the confinement should not change the ground-state.

C. Finite-element discretization

In the finite-element method the computational domain Ω is divided into small, polyhedral regions called elements. This division is denoted by $\mathcal{T}_h$. For our purposes it is sufficient to use tetrahedra. Other popular choices are hexahedra, pyramids, and prisms. The division of Ω is handled by an external mesh-generator that can either (i) generate the mesh for a given geometry or (ii) calculate the Delaunay tetrahedralization of a given set of points. We have chosen the latter option and the points for the mesh are generated as specified in Sec. II C 1.

Once the division of the domain Ω is complete the space of approximation, V_h, can be defined. For the finite-element method this is taken to be continuous, piecewise polynomial functions, i.e.,

$$V_h = \{v_h \in C(\Omega) | (v_h)_{|K} \in \Pi_p\} \quad \forall\, K \in \mathcal{T}_h, \tag{19}$$

where K is an element, Π_p denotes polynomials of order p, h refers to the size of the elements in the mesh, and $C(\Omega)$ refers to continuous functions in the domain. In general, the order p can vary from one element to another as long as the continuity condition $v_h \in C(\Omega)$ is respected but in our calculations we choose to keep p fixed throughout the mesh. The value of p decides if the method is considered to be of high-order and the usual requirement is $p>3$ for a high-order method. Also, if the convergence is obtained via increasing the order of polynomials rather than refining the mesh, the method is called the p-method. The mesh refinement approach gives an h-method and combining these approaches leads to an hp-method.[35]

Next, a basis for the space V_h must be chosen. The canonical way for the high-order method is to divide the local basis functions of a single element into four disjoint sets: nodal functions, edge functions, face functions, and bubble functions. The nodal functions are first order polynomials that have a value of 1 at one of the vertices and 0 at others. The edge functions are polynomials up to an order p and they are nonzero only on one of the edges of the element. The face functions are similar to the edge functions but they are in correspondence with the faces of the element. Finally, the bubble functions are zero on all the vertices, edges and faces of the element but nonzero inside the element. The actual basis functions are generated using products of one-dimensional integrated Legendre polynomials over the interval $[-1,1]$. Note that due to the continuity requirements the basis functions actually extend over several elements that share the same geometrical feature (see Fig. 1).

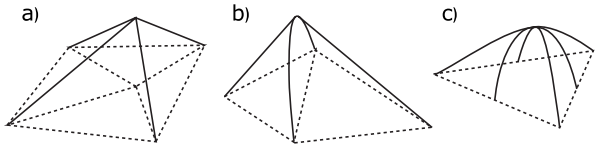

FIG. 1. Schematic view of finite-element basis functions in 2D: (a) vertex, (b) edge, and (c) bubble basis functions.

In practice, the basis functions for an element K in the mesh are generated using a reference element, $\hat{K}$, and (affine) mappings $F:\hat{K}\rightarrow K$. Then the basis functions on an element K can be written as images of the basis functions on the reference element, i.e.,

$$\varphi(\mathbf{r}) = \hat{\varphi}[F^{-1}(\mathbf{r})], \tag{20}$$

reducing the programming effort to $\hat{K}$.

Once the basis $\{\phi_j\}_{j=1}^{N_b}$ for the space V_h is ready for use an approximation to the Kohn–Sham[30] orbitals can be looked for in the form $\psi_k(\mathbf{r})=\sum_{j=1}^{N_b} c_j^k \phi_j(\mathbf{r})$. There are many ways to find the coefficients c_i but in the finite-element method the variational approach is used. This leads to an equation for the state k

$$\sum_{j=1}^{N_b} \langle \phi_i | \hat{H}_{\mathrm{KS}} | \phi_j \rangle c_j^k = \epsilon_k \sum_{j=1}^{N_b} \langle \phi_i | \phi_j \rangle c_j^k, \quad i = 1, \ldots, N_b, \tag{21}$$

that reads in matrix form as

$$Hc^k = \epsilon_k S c^k, \tag{22}$$

where

$$H_{ij} = \langle \phi_i | \hat{H}_{\mathrm{KS}} | \phi_j \rangle, \quad S_{ij} = \langle \phi_i | \phi_j \rangle = \int_{\mathbb{R}^3} \phi_i(\mathbf{r}) \phi_j(\mathbf{r}) d\mathbf{r}. \tag{23}$$

A few observations are in order. First, since the finite-element basis functions are strictly localized in space the matrices H and S are sparse. This not only allows for, but also actually dictates the use of sparse matrix technologies. Second, if the domain Ω is large enough so that selecting the zero boundary conditions on $\partial\Omega$ is justified the variational formulation (21) holds and consequently the matrix H is also symmetric. In this case the fact that the basis functions ϕ_i don't have continuous derivatives across the element borders is not an obstacle since in Eq. (21) only a square integrable gradient is required for the basis functions [see Eq. (8)].

1. Mesh generation

The mesh is generated by merging structured atomic meshes to a molecular mesh. The nodes of atomic meshes consist of layers of vertices of polyhedra. The radius of the layer r_k is changed as $r_k=q^k r_0$ with r_0 and q as parameters, and $k \subset \mathbb{Z}$ $(-n \leq k \leq m; n, m \subset \mathbb{N})$. The choice of polyhedra is arbitrary, but they should provide tetrahedra of good quality (our quality requirements are explained below in this section). We have chosen to use deltoidal icositetrahedron and its dual, rhombicuboctahedron, both shown in Fig. 2.

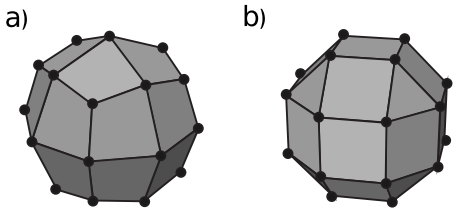

FIG. 2. Polyhedra used in atomic meshes of (a) deltoidal icositetrahedron and (b) rhombicuboctahedron.

The zeroth layer is chosen relative to the size of the highest occupied atomic orbital $r_0=(2I)^{-1/2}/4$, where I is the first ionization energy. The layers with negative indices are created until the radius of the layer is of the order of the lowest state $r_{k_{\min}}<Z_a^{-1}/128$. The factors 1/4 and 1/128 are somewhat arbitrary at the moment, but are sufficient for systems under study. If necessary one extra layer is added, as the last layer should be deltoidal icositetrahedron to ensure good quality of the elements around the nuclei. The inner part of the mesh is finalized by adding one node to the nucleus $\mathbf{R}_a$.

The nodes of the layers with positive indices are added only if the node is inside the atomic mesh region, i.e., not in the molecular mesh region. The node of atom a is in the molecular region if

$$g_{ab}|\mathbf{R}_b-\mathbf{R}_a|/|\mathbf{r}-\mathbf{R}_a|-\frac{\mathbf{r}-\mathbf{R}_a}{|\mathbf{r}-\mathbf{R}_a|}\cdot\frac{\mathbf{R}_b-\mathbf{R}_a}{|\mathbf{R}_b-\mathbf{R}_a|}<\beta(q-1), \tag{24}$$

for all other nuclei b, where $g_{ab}=r_0^a/(r_0^a+r_0^b)$ are the relative sizes with respect to the other nuclei, and β is chosen to be 1/3. In practice, this procedure creates an empty space between atoms, which reaches closer to smaller atoms than larger ones, and its thickness is proportional to the distance between the closest pair of atoms. For each pair of atoms the atomic regions are inside two halves of an elliptical hyperboloid.

The nodes for the molecular mesh region are then created by first adding a spherical layer of nodes around the center of atomic charges $\mathbf{R}_{cc}$. The layer forms the boundary of the simulation cell and has a radius equal to $r_{\partial\Omega}=q\max_i|\mathbf{r}_i-\mathbf{R}_{cc}|$, the radius of the furthest node from the center of atomic charged multiplied by the layer ratio q. Then an initial molecular mesh is created by a Delaunay tetrahedralization[36] of the nodes (see Fig. 3). The molecular mesh is then refined by Delaunay refinement,[37] i.e., by inserting nodes at the circumcenters (the center of circumsphere) of too large elements one at the time and repeating Delaunay tetrahedralization after each insertion. An element

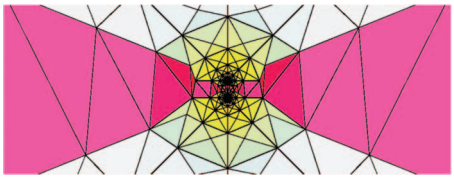

FIG. 3. Initial molecular mesh for the CO molecule before refinement and improvement. The elements of the molecular region are shown in pink.

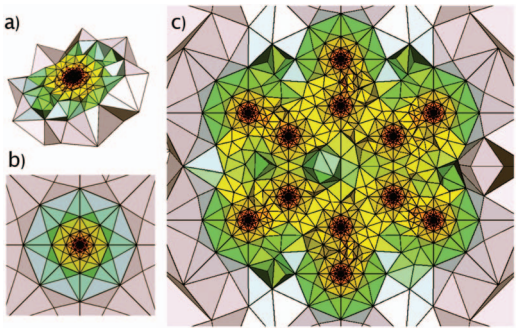

FIG. 4. Cut plane of the molecular mesh of the C_6H_6 molecule with parameters $q=\sqrt{2}$, $s\geq\sqrt{1/3}$, and 15 outer layers (see text): (a) the complete mesh (diameter of 55 Å), (b) the atomic mesh near a carbon nucleus, and (c) the close-up of the molecular region.

is deemed too large, if its longest edge is longer than the longest edge of an element in the atomic mesh with the same distance from the closest atom. Or, if its average edge length is longer than the average edge length of an element in the atomic mesh with the same distance from the closest atom. (Obviously, the elements, which are connected to the nuclei, are ignored.) After refining the mesh to fill the size constraints, the quality of the elements is ensured. All elements with too small a ratio $s=\sqrt{3}r_{\text{in}}/r_{\text{circ}}$, where r_{in} is the radius of the inscribing sphere, and r_{circ} is the radius of the circumsphere, are Delaunay refined as above until no elements with low quality are present. Keeping the ratio s relatively close to one will ensure that all angles (dihedral and face) are neither too large nor too small.[38,39] This is one of the standard measures for the quality of an element. The elements which are connected to the boundary nodes are not currently being refined. However, the quality of these elements is not very important because the solution is practically zero in this region.

The resulting molecular mesh is somewhat finer than the atomic meshes, but because the main interest is in the molecular region, we consider it justified to slightly overdiscretize this region. An example of a molecular mesh for benzene C_6H_6 with $q=\sqrt{2}$, $s=\sqrt{1/3}$, and 15 outer layers is shown in Fig. 4. The diameter of mesh is 55 Å.

D. Implementation

Our current implementation is based on the ELMER finite-element software package,[40] and the Delaunay tetrahedralization is done using TETGEN.[41,42] The ground-state Kohn–Sham[30] system was solved with the self-consistent iteration scheme. The locally optimal block preconditioned conjugated gradient[43] method was applied to the linearized Kohn–Sham[30] eigenvalue problem [Eq. (8)], and the convergence rate of the nonlinear system was enhanced with the Pulay mixing[44] procedure for the density. The electronic charge was compensated by Gaussian countercharges at nuclei in the Poisson equation [Eq. (9)], and then a canceling potential for the counter-charges was added in the assembly of the Hamiltonian matrix [in Eq. (21)]. Preconditioner for the eigenvalue problem was chosen to be the incomplete Cholesky factorization[45] for $T+\alpha S$, where T is the kinetic energy operator and α was chosen to be 13.6 eV.

TABLE I. Total energies of H, C, and O atoms calculated using elements with degrees $p=2-4$.

	E_{LDA} (eV)		
	H	C	O
$p=2$	−12.0509	−1011.1067	−2011.1970
$p=3$	−12.1245	−1018.1042	−2025.8759
$p=4$	−12.1271	−1018.3581	−2026.4268
FHI-aims	−12.127	−1018.369	−2026.451

TABLE II. Total energies of H_2, CO, and C_6H_6 molecules calculated using elements with degrees $p=2-4$.

	E_{LDA} (eV)		
	H_2	CO	C_6H_6
$p=2$	−30.8407	−3039.5322	−6226.5746
$p=3$	−30.9510	−3059.7776	−6262.5718
$p=4$	−30.9542	−3060.5009	−6263.7841
FHI-aims	−30.954	−3060.529	−6263.829

In the linear-response calculation, the main effort is in calculating the integrals of the matrix elements in Eq. (15). Each row of the matrix is independent of the other rows, and thus the problem is trivial to parallelize over the rows of the matrix. Also, some of the matrix elements (and rows) can be ignored beforehand as their eigenvalue difference is clearly outside the relevant energy interval, e.g., transitions from core states. The exchange-correlation kernel $f_{\mathrm{xc}}(\mathbf{r},\mathbf{r}',\omega)$ requires the second functional derivative of the exchange-correlation functional with respect to the density. However, when the second derivative is not available, the finite-difference approximation

$$\int d^3\mathbf{r}\frac{\delta E_{\mathrm{xc}}}{n(\mathbf{r})n(\mathbf{r}')}n_{jk}(\mathbf{r}') = \lim_{\Delta\to 0}\frac{v_{\mathrm{xc}}[n+\Delta n_{jk}](\mathbf{r})-v_{\mathrm{xc}}[n-\Delta n_{jk}](\mathbf{r})}{2\Delta}, \tag{25}$$

can be used. Above,

$$n_{jk}(\mathbf{r}) = \psi_j^*(\mathbf{r})\psi_k(\mathbf{r}), \tag{26}$$

is the pair density.

III. RESULTS AND DISCUSSION

We demonstrate our ground-state DFT and linear-response TDDFT methods by applying them to atoms and small molecules. We calculated hydrogen, carbon, and oxygen atoms, and hydrogen, carbon monoxide, and benzene molecules. We calculated optical absorption spectra for a beryllium atom, sodium dimer, and benzene molecule. The convergence properties are discussed in both cases.

A. Ground-state DFT

We applied the local density approximation (LDA) functional with the Perdew–Wang parametrization[46] in all calculations, and all results are for spin-compensated systems. In all calculations, the simulation cell diameter was approximately 50 Å, and the geometrical coarsening factor $q=\sqrt{2}$.

The total energies of the atoms and molecules calculated with increasing polynomial degree are shown in Tables I and II, and the atomization energies of the molecules in Table III. We have used for H_2 and CO the bond lengths of 0.75 and 1.1 Å, respectively. C_6H_6 has a planar geometry with atomic positions of C: (0.000, ±1.396) Å, (±1.209, ±0.698) Å, and H: (0.000, ±2.479) Å, (±2.147, ±1.240) Å used. The H_2 mesh had 12×10^3, 41×10^3, and 96×10^3 DOFs; the CO mesh had 14×10^3, 46×10^3, and 109×10^3 DOFs; and the C_6H_6 mesh had 59×10^3, 199×10^3, and 470×10^3 (DOFs), for element degrees $p=2$, $p=3$, and $p=4$, respectively. The corresponding results calculated with very high accuracy (~1 meV) using the electronic structure program FHI-aims[7] are shown on the last rows of the tables. As one can see, the total energy requires a high polynomial degree ($p>3$) to converge within an error below 100 meV. However, in practice one is interested in the atomization energy of the system, which is the difference of the total energies between the system and the corresponding isolated atoms. The cancellation of errors leads to a significant improvement in the accuracy, and already the 2nd and 3rd degree polynomials produce results with errors around 100 and 10 meV, respectively. The maximal cancellation was obtained by using the same mesh for isolated atoms as for the molecule, which can be considered as a kind of a basis set superposition error, (i.e., a counterpoise) correction.[47] The energies of the isolated atoms are lower in the molecular mesh than in the atomistic mesh. This is because the molecular mesh is denser than the atomistic mesh as one wants to guarantee the good description of the bonding regions. The total and atomization energies are well converged with respect to the simulation cell diameter. We found less than 1 meV difference in range from 21 to 151 Å for the CO molecule.

We performed nonrelativistic calculations for elements Zn, I, Hg, and At in order to test the quality of the discretization in the case of heavy elements. We found that elements with *d*-electrons perform relatively well, e.g., the atomization energy of the I_2 molecule (−2.400, −3.015, and −3.031 eV, for $p=2,3,4$, respectively, and −3.037 eV for FHI-aims) has approximately two to four times larger errors than the C_6H_6 molecule. Elements with *f*-electrons perform much worse, e.g., At_2 has one order of magnitude larger errors than C_6H_6 molecule. This is due to insufficient angular DOFs as the eigenvalues of the *f*-orbitals split (and *d*-orbitals split slightly) in energy, whereas *p*-orbitals do not. Our estimate is that one would need ~2–4 times more angular DOFs for

TABLE III. Atomization energies of H_2, CO, and C_6H_6 molecules calculated using elements with degrees $p=2-4$.

	ΔE_{LDA} (eV)		
	H_2	CO	C_6H_6
$p=2$	−6.6838	−15.7573	−81.0894
$p=3$	−6.6996	−15.7162	−80.8599
$p=4$	−6.6999	−15.7114	−80.8541
FHI-aims	−6.700	−15.709	−80.852

TABLE IV. Atomization energy of the CO molecule at different bond lengths calculated using elements with degrees $p=2-4$.

	ΔE_{LDA} (eV)			
R_{CO} (Å)	$p=2$	$p=3$	$p=4$	FHI-aims
0.8	−0.1272	−0.6514	−0.6648	−0.660
1.0	−14.4446	−14.4495	−14.4464	−14.444
1.1	−15.7584	−15.7175	−15.7115	−15.709
1.2	−15.6235	−15.4910	−15.4845	−15.482
1.4	−13.5165	−13.3027	−13.2934	−13.292
1.8	−8.5848	−8.3963	−8.3875	−8.386
2.4	−4.0303	−3.9093	−3.9043	−3.903

heavy elements, which in addition to ~50% more radial DOFs is ~3–6 times more DOFs than for carbon.

Tables IV and V show the convergence of the potential energy surface and the dipole moment, respectively, calculated with elements with degrees $p=2-4$. The potential energy surface shows no "egg-box effect," known to exists in uniform real-space grids.[48] However, there exists a similar kind of effect. For example in a diatomic molecule, when the bond length is changed, new elements are created into or old ones are removed from the mesh. In improperly generated meshes, this can cause severe problems as the potential energy surface may have significant artificial oscillations and discontinuities. For this reason, we recommend a slightly denser discretization of the bonding regions compared to the atomic regions. Based on our experimentations on diatomic molecules, this is sufficient and forces with a quality comparable to that from commonly used codes, such as the real-space code GPAW,[13] are obtained.

Note that we have given two different values for the atomization energy of CO at the bond length of $R_{\mathrm{CO}}=1.1$ Å for each element degree p (see Tables III and IV). Because the mesh generation is not unique for a given molecule but rather for given Cartesian positions and the order in which the atoms are given, the difference is due to different meshes obtained from two different generator inputs. However, the difference is one order of magnitude smaller than the error in the atomization energy. The dipole moment shows errors less than 0.01 and 0.001 eÅ when using 2nd and 3rd order polynomials, respectively.

In Table VI, we show the Kohn–Sham[30] eigenvalues of the C_6H_6 molecule. The core eigenvalues exhibit much larger absolute errors than the valence eigenvalues, but the relative errors are of same order. The valence eigenvalues converge similarly to the atomization energies, which is reasonable as the errors in the core eigenvalues cancel when taking the differences. The remaining error is mainly due to the valence states and the molecular orbitals which they form.

TABLE V. Dipole moment of the CO molecule at different bond lengths calculated using elements with degrees $p=2-4$.

	μ_{LDA} (eÅ)			
R_{CO} (Å)	$p=2$	$p=3$	$p=4$	FHI-aims
0.8	0.2454	0.2402	0.2400	0.2398
1.0	0.1390	0.1311	0.1307	0.1305
1.1	0.0745	0.0669	0.0666	0.0663
1.2	0.0064	−0.0010	−0.0013	−0.0015
1.4	−0.1330	−0.1397	−0.1399	−0.1399
1.8	−0.3792	−0.3792	−0.3791	−0.3790
2.4	−0.6084	−0.5996	−0.5992	−0.5991

TABLE VI. Kohn–Sham orbital energies (eigenvalues) of the C_6H_6 molecule calculated using elements with degrees $p=2-4$.

	ϵ_{LDA} (eV)			
State	$p=2$	$p=3$	$p=4$	FHI-aims
1	−264.6616	−266.3819	−266.4388	−266.4382
⋯				
6	−264.6087	−266.3585	−266.4156	−266.4150
7	−21.1552	−21.1155	−21.1557	−21.1560
8	−18.3474	−18.3608	−18.3616	−18.3619
9	−18.3404	−18.3597	−18.3609	−18.3612
⋯				
18	−8.2867	−8.2915	−8.2915	−8.2917
19	−8.2839	−8.2895	−8.2895	−8.2897
20	−6.5401	−6.5341	−6.5343	−6.5338
21	−6.5385	−6.5339	−6.5342	−6.5338

B. Linear-response TDDFT

For the linear-response TDDFT calculations we used actually a slightly different mesh generation scheme than that described above in Sec. I. This old scheme, developed also by us, uses (i) different alternating polyhedra, i.e., tetrakis hexahedron and slightly compressed (larger cubic faces) truncated cuboctahedron, for atomic meshes, and (ii) different quality measures, i.e., dihedral angles and aspect ratio (longest edge/smallest side height), than the current one. Compared to the old one, the current mesh generation scheme is simpler and it produces higher quality atomic meshes. However, the difference in quality is negligible when applying to the linear-response TDDFT.

First, we consider a simple test system, a beryllium atom, to demonstrate the convergence properties. We begin with the polynomial degrees $p=2$ and $p=3$, 150 states, the confinement radius $R_c=8.0a_0$, and the force constant $k_c=10^{-3}E_h/a_0^2$. The resulting spectra are shown in Fig. 5. Increasing the polynomial degree of the elements has only a small effect of ~20 meV for the first peak position, and of ~70 meV for the second peak position ($h\nu_{p=3}>h\nu_{p=2}$). The effect of different confinement potentials can be seen in Figs. 6 and 7. A stronger confinement provides a faster conver-

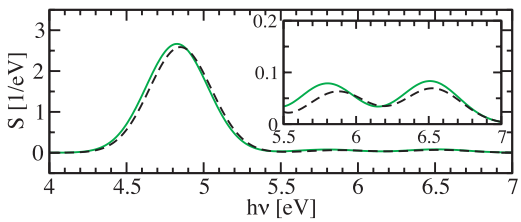

FIG. 5. Optical absorption spectra of the beryllium atom calculated using elements with degrees $p=2$ (solid) and $p=3$ (dashed). The inset shows a magnification of the high-energy region.

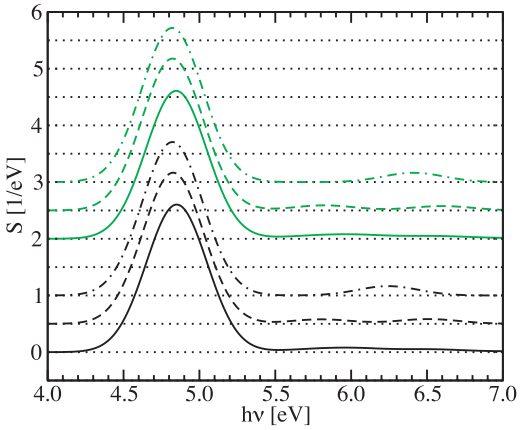

FIG. 6. Optical absorption spectrum of the beryllium atom calculated using the confinement potential parameters (from the highest curve to the lowest one): $k_c=10^{-2}E_h/a_0^2$, $R_c=4.0a_0$; $k_c=10^{-3}E_h/a_0^2$, $R_c=4.0a_0$; $k_c=10^{-4}E_h/a_0^2$, $R_c=4.0a_0$; $k_c=10^{-2}E_h/a_0^2$, $R_c=8.0a_0$; $k_c=10^{-3}E_h/a_0^2$, $R_c=8.0a_0$; and $k_c=10^{-4}E_h/a_0^2$, $R_c=8.0a_0$. The spectra are separated by shifting the zero level.

gence with respect to the number of states, but at the same time, the converged transition energies are shifted to slightly higher energies. A weaker confinement provides energies which are better converged, but the convergence may not be reached with the available number of states, as in the case of $k_c=10^{-4}E_h/a_0^2$ in Fig. 7. In Fig. 6, the number of states was increased to 250 which yields an error less than 30 meV s. Obviously, the transitions at higher energies are more sensitive to confinement than transitions at low energies. The convergence with respect to the number of states included in the calculation is not smooth, but rather has a step every time a new state contributing to the transition is included in the basis. The step is not always smaller than the previous one, and it can be hard to decide whether the spectrum has converged by observing the convergence with respect to the number of states.

Next, we examined two molecular test systems, the sodium dimer Na_2 and the benzene molecule C_6H_6. The simulated photoabsorption spectrum of the Na_2 is shown in Fig. 8. The calculation included 250 states, and two different confinement potentials were used: one with $R_c=8.0a_0$ and $k_c=10^{-2}E_h/a_0^2$, and one with $R_c=8.0a_0$ and $k_c=10^{-3}E_h/a_0^2$. Practically, the same result of 2.15 eV was obtained for the first peak with the two sets of parameters. For the second one there is a small shift from 2.69 to 2.72 eV. In contrast, the third clearly visible peak in the spectrum shows a remarkable shift from 3.4 to 4.3 eV.

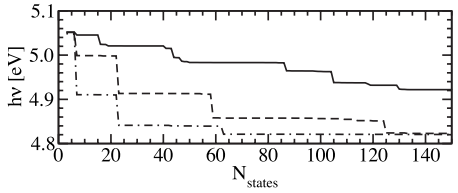

FIG. 7. Convergence of the position of the first transition peak in the optical absorption spectrum of the beryllium atom with respect to the number of states included in the calculation. The confinement potential parameters used are: $k_c=10^{-2}E_h/a_0^2$, $R_c=4.0a_0$ (dash-dotted); $k_c=10^{-3}E_h/a_0^2$, $R_c=4.0a_0$ (dashed); and $k_c=10^{-4}E_h/a_0^2$, $R_c=4.0a_0$ (solid).

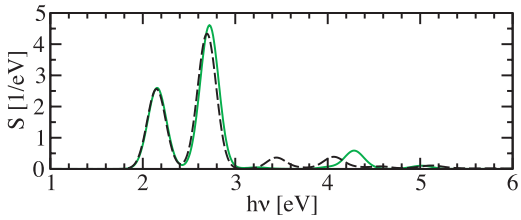

FIG. 8. Optical absorption spectra of the sodium dimer calculated with the confinement potential parameters of $k_c=10^{-2}E_h/a_0^2$, $R_c=8.0a_0$ (solid) and $k_c=10^{-3}E_h/a_0^2$, $R_c=8.0a_0$ (dashed).

The photoabsorption spectrum of the benzene molecule is shown in Fig. 9. Again two different confinement potentials were used, one with $R_c=4.0a_0$ and $k_c=10^{-2}E_h/a_0^2$, and one with $R_c=4.0a_0$ and $k_c=10^{-3}E_h/a_0^2$. The spectrum with the weaker confinement ($k_c=10^{-3}$) is not converged yet with 250 states, which corresponds already nearly 4 million matrix elements. The spectrum with the stronger confinement and 150 states is converged in the lower energy part of the spectrum, and reproduces correctly the main experimental peak around 7 eV. It also shows the beginning of a broad feature above 9 eV in agreement with the experiment.

C. Computational details

The ground-state DFT calculations were performed as serial calculations, and the time consumed ranged from minutes (hydrogen atom) to tens of hours (benzene with $p=4$). All calculations were done on 2.6 GHz AMD Opteron dual-core processors. As the systems were relatively small, the storage requirements of the matrices were much larger than those of the wave functions. The number of nonzero entries in the matrices ranged from 1×10^5 (H, $p=2$) to 4×10^7 (C_6H_6, $p=4$). The number of DOFs ranged from 5000 (H, $p=2$) to 5×10^5 (C_6H_6, $p=4$). The linear-response TDDFT was parallelized over the rows of the Casida matrix, and the absorption spectrum of benzene was calculated using several hundreds of processors.

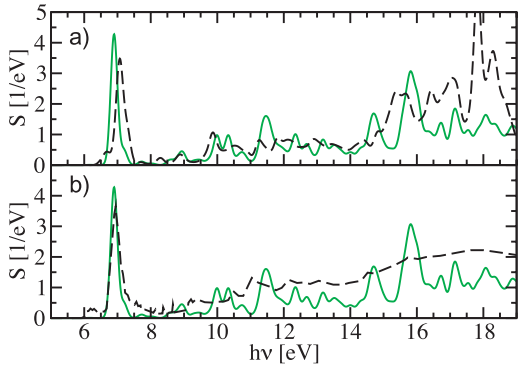

FIG. 9. Optical absorption spectra of the benzene molecule: (a) the spectra calculated using the confinement potential parameters $k_c=10^{-2}E_h/a_0^2$, $R_c=4.0a_0$ (solid) and $k_c=10^{-3}E_h/a_0^2$, $R_c=4.0a_0$ (dashed); (b) the spectrum calculated using the confinement potential parameters $k_c=10^{-2}E_h/a_0^2$, $R_c=4.0a_0$ (solid) and the experimental spectrum (Ref. 49) (dashed).

We consider the performance attained adequate for an initial "proof-of-concept" implementation. Moreover, we expect to increase the speed substantially by employing more sophisticated methods. Especially, the preconditioning of the eigenvalue problem and improved initial guesses for Kohn–Sham[30] wave functions are expected to result in remarkable improvements.

IV. CONCLUSIONS

We have described and implemented a high-order hierarchical finite-element method on unstructured meshes for all-electron DFT and TDDFT method. Our finite-element mesh generation scheme assures the quality of the elements in the mesh by merging high-quality, structured atomic meshes to an initial molecular mesh, which is then refined to meet the size and shape requirements by applying the Delaunay refinement method. The ground-state DFT calculations were performed using elements with degrees $p=2-4$, which provide increasing levels of accuracy down to a few meV s.

We also described a flexible way to construct a basis for the finite-element linear-response TDDFT calculation. By applying an auxiliary confinement potential to the ground-state calculation, the basis can be tuned to balance between accuracy and computational cost. The convergence properties of the optical absorption spectrum were discussed in the cases of the beryllium atom, and the sodium dimer and benzene molecules.

The initial implementation has proved the applicability of the hierarchical finite-element method on unstructured meshes to all-electron DFT and TDDFT. However, there exist several open questions which must be further studied and improved, for example, the preconditioning of the eigenvalue problem. As the finite-element method is well-suited for the domain decomposition, the parallel implementation would provide access to much larger systems within reasonable execution times. As most of the applications do not need full all-electron solutions, the projector-augmented wave method or a similar treatment should speed up calculations remarkably in these cases. Magnetic fields, relativistic effects, and quantum mechanical forces for atoms will be implemented in order to broaden the applicability of the method. Finally, we believe that the most promising application areas for our method are beyond the ground-state and linear-response calculations, for example, in the time-propagation TDDFT scheme.

ACKNOWLEDGMENTS

This work was performed in COMP which is Center of Excellence of Academy of Finland, and was funded by a grant from CSC-IT Center for Science Ltd., AMD, and Cray. The calculations were performed using CSC's resources. L.L. wishes to thank Mikko Lyly and the rest of CSC's Elmer team for support with Elmer, as well as Harri Hakula for advices on mesh generation. ELMER is an open source finite element software for multiphysical problems developed and supported by CSC.

[1] W. Kohn, Rev. Mod. Phys. **71**, 1253 (1999).
[2] P. Hohenberg and W. Kohn, Phys. Rev. **136**, B864 (1964).
[3] *A Primer in Density Functional Theory*, edited by C. Fiolhais, F. Nogueira, and M. Marques (Springer-Verlag, New York, 2003).
[4] R. G. Parr and W. Yang, *Density-Functional Theory of Atoms and Molecules* (Oxford University Press, New York, 1989).
[5] P. Elliott, F. Furche, and K. Burke, Rev. Comput. Chem. **26**, 91 (2008).
[6] E. Runge and E. K. U. Gross, Phys. Rev. Lett. **52**, 997 (1984).
[7] V. Blum, R. Gehrke, F. Hanke, P. Havu, V. Havu, X. Ren, K. Reuter, and M. Scheffler, Comput. Phys. Commun. DOI:10.106/j.cpc.2009.06.022 (2008).
[8] M. J. Frisch *et al.*, GAUSSIAN03, Gaussian, Inc., Wallingford, CT, 2004.
[9] J. M. Soler, E. Artacho, J. D. Gale, A. García, J. Junquera, P. Ordejon, and D. Sanchez-Portal, J. Phys.: Condens. Matter **14**, 2745 (2002).
[10] X. Gonze, J.-M. Beuken, R. Caracas, F. Detraux, M. Fuchs, G.-M. Rignanese, L. Sindic, M. Verstraete, G. Zerah, F. Jollet, M. Torrent, A. Roy, M. Mikami, Ph. Ghosez, J.-Y. Raty, and D. C. Allan, Comput. Mater. Sci. **25**, 478 (2002).
[11] G. Kresse and J. Hafner, Phys. Rev. B **47**, 558 (1993).
[12] M. A. L. Marques, A. Castro, G. F. Bertsch, and A. Rubio, Comput. Phys. Commun. **151**, 60 (2003).
[13] J. J. Mortensen, L. B. Hansen, and K. W. Jacobsen, Phys. Rev. B **71**, 035109 (2005).
[14] E. Fermi, Nuovo Cimento **11**, 157 (1934).
[15] J. C. Phillips and L. Kleinman, Phys. Rev. **116**, 287 (1959).
[16] N. Troullier and J. L. Martins, Phys. Rev. B, **43**, 1993 (1991).
[17] P. E. Blöchl, Phys. Rev. B **50**, 17953 (1994).
[18] B. Szabo and I. Babuska, *Finite Element Analysis* (Wiley, New York, 1991).
[19] M. J. Turner, R. W. Clough, H. C. Martin, and L. J. Topp, J. Aeronaut. Sci. **23**, 805 (1956).
[20] K.-J. Bathe, *Finite Element Procedures (Part 1-2)*, 2nd ed. (Prentice-Hall, Englewood Cliffs, NJ, 1995).
[21] P. F. Batcho, Phys. Rev. A **57**, 4246 (1998).
[22] P. F. Batcho, Phys. Rev. E **61**, 7169 (2000).
[23] J.-L. Fattebert, R. D. Hornunga, and A. M. Wissink, J. Comput. Phys. **223**, 759 (2007).
[24] F. S. Levin and J. Shertzer, Phys. Rev. A **32**, 3285 (1985).
[25] J. E. Pask and P. A. Sterne, Modell. Simul. Mater. Sci. Eng. **13**, R71 (2005).
[26] E. Tsuchida and M. Tsukada, Phys. Rev. B **52**, 5573 (1995).
[27] S. R. White, J. W. Wilkins, and M. P. Teter, Phys. Rev. B **39**, 5819 (1989).
[28] Yu. Hengtai and D. Andre, J. Chem. Phys. **102**, 1257 (1994).
[29] D. Zhang, L. Shen, A. Zhou, and X.-G. Gong, Phys. Lett. A **372**, 5071 (2008).
[30] W. Kohn and L. J. Sham, Phys. Rev. **140**, A1133 (1965).
[31] S. C. Brenner and L. R. Scott, *The Mathematical Theory of Finite Element Methods* (Springer, New York, 2008).
[32] K. Yabana and G. F. Bertsch, Phys. Rev. B **54**, 4484 (1996).
[33] M. E. Casida, in *Recent Developments and Applications in Modern Density-Functional Theory*, edited by J. M. Seminario (Elsevier, Amsterdam, 1996), p. 391.
[34] M. E. Casida, in *Recent Advances in Density Functional Methods, Part I*, edited by D. P. Chong (World Scientific, Singapore, 1995), p. 155.
[35] Ch. Schwab, *p - and hp*-Finite Element Methods (Clarendon/Oxford University Press, New York, 1998).
[36] M. Bern and D. Eppstein, in *Computing in Euclidean Geometry*, 2nd ed., edited by D.-Z. Du and F. K. Hwang (World Scientific, Singapore, 1995), pp. 47–123.
[37] J. R. Shewchuk, "Delaunay Refinement Mesh Generation," Ph.D. thesis, Carnegie Mellon University, 1997; J. R. Shewchuk, Technical Report No. CMU-CS-97-137, 1997.
[38] J. C. Cavendish, D. A. Field, and W. H. Frey, Int. J. Numer. Methods Eng. **21**, 329 (1985).
[39] J. R. Shewchuk, What is a good linear finite element? Interpolation, conditioning, anisotropy, and quality measures. http://www.cs.berkeley.edu/jrs/papers/elemj.pdf, 2002. unpublished preprint.
[40] CSC IT Center for Science, ELMER, open source finite element software for multiphysical problems, http://www.csc.fi/english/pages/elmer.
[41] H. Edelsbrunner and N. R. Shah, Algorithmica **15**, 223 (1996).
[42] H. Si, TETGEN, three-dimensional Delaunay triangulator. http://tetgen.berlios.de/.

[43] A. Knyazev, SIAM J. Sci. Comput. (USA) **23**, 517 (2001).
[44] P. Pulay, Chem. Phys. Lett. **73**, 393 (1980).
[45] G. H. Golub and C. F. Van Loan, *Matrix Computations*, 2nd ed. (The Johns Hopkins University Press, Baltimore, MD, 1993), pp. 530–531.
[46] J. P. Perdew and Y. Wang, Phys. Rev. B **45**, 13244 (1992).
[47] S. F. Boys and F. Bernardi, Mol. Phys. **19**, 553 (1970).
[48] T. Ono and K. Hirose, Phys. Rev. Lett. **82**, 5016 (1999).
[49] E. E. Koch and A. Otto, Chem. Phys. Lett. **12**, 476 (1972).